Vat photopolymerization of bio-derived conductive composites for smart devices with Joule heating capabilities

Progress in Additive Manufacturing (2026) 11:5197–5216
https://doi.org/10.1007/s40964-026-01541-x

RESEARCH

Vat photopolymerization of bio-derived conductive composites for smart devices with Joule heating capabilities

Alberto Cellai[1] · Lorenzo Pezzana[1] · Kimihiro Matsukawa[2] · Alberto Jiménez-Suárez[3,4] · Marco Sangermano[1] · Alejandro Cortés[3]

Received: 15 September 2025 / Accepted: 13 January 2026 / Published online: 2 April 2026

Abstract

This study explores the use of a bio-based photopolymerizable monomer, acrylate polyglycerol, for fabricating smart 3D-printed objects Vat Photopolymerization (VPP) technology. Derived from vegetable oil saponification or microbial fermentation, this monomer serves as a photocurable building block after acrylate functionalization. Conductive fillers, including silver, copper, nickel powders, and mechanically recycled carbon fibers (RCF), were incorporated to enhance electrical conductivity and Joule heating capabilities. These formulations combine the sustainability of bio-derived materials with advanced functionalities for smart applications. Characterization techniques such as FT-IR, photo-DSC, rheology, DMTA, electrical conductivity analysis, and thermal imaging revealed that while increasing filler content reduces polymerization rate and increases viscosity, it significantly improves electrical conductivity and, in some cases, thermal-mechanical properties. Notably, Ag- and RCF-filled formulations enabled effective Joule heating, achieving uniform heat distribution. As a proof-of-concept, a smart wearable ring was 3D-printed using a 50%wt Ag formulation, reaching therapeutic temperatures (60 °C) with minimal energy input (1–3 V). The ability to manufacture geometrically complex, energy-efficient devices through 3D printing, combined with the sustainability of bio-based resins, highlights the potential of these materials for medical, electronic, and smart applications. This research bridges sustainability and innovation in additive manufacturing, paving the way for high-performance, eco-friendly solutions.

Graphical abstract

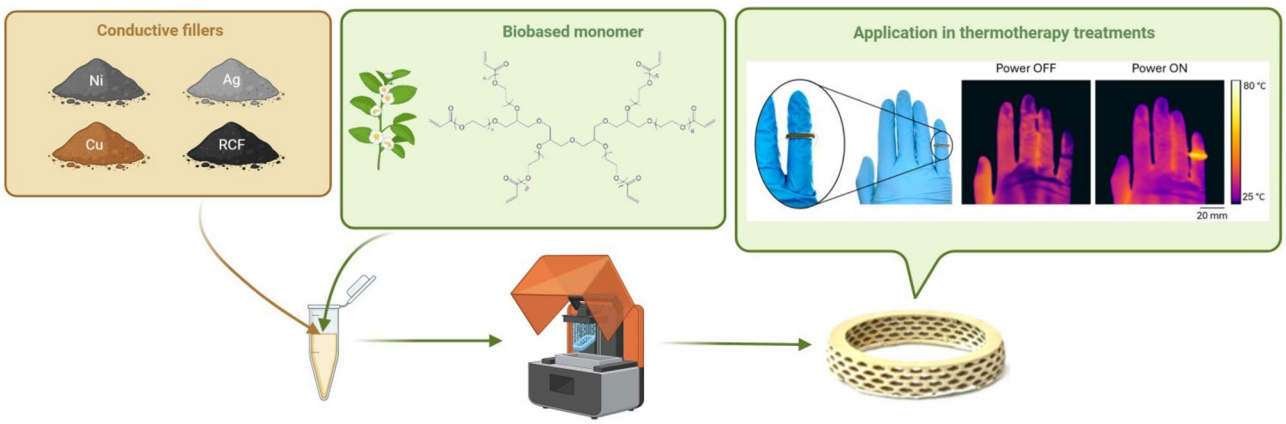

Keywords Vat photopolymerization · Bio-based · Smart materials · Joule heating · Thermotherapy

Extended author information available on the last page of the article

1 Introduction

Achieving sustainable development is one of the major challenges of the current era, as highlighted by the UN's 2030 Agenda [1, 2]. A key goal is the reduction of climate change through decreased reliance on fossil fuels, reduced greenhouse gas emissions, and minimized carbon footprint. In this context, the transition from fossil-based to bio-based polymers is crucial, as bio-based polymers represent natural alternatives to conventional plastics, offering a promising route toward sustainable production [3–5].

Besides the choice of precursors, the processing method must also be considered. UV-curing is among the most sustainable consolidation techniques for polymers due to its low VOC emissions, high efficiency, and reduced energy consumption compared to thermal processes [6, 7]. It is already widely applied in adhesives, coatings, inks, and sectors from electronics to dentistry [8–10]. More recently, UV-curing has been extended to additive manufacturing (AM), enabling material-efficient production with minimal waste [11, 12]. Among AM techniques, VAT Photopolymerization (VPP) is the most suitable for liquid resins, where stereolithography (SLA) and digital light processing (DLP) are the leading approaches [13–16].

Combining bio-based photocurable precursors with AM technologies is an effective strategy to reduce energy consumption and fossil-derived polymers [17, 18]. Several bio-based UV-curable resins have been reported, including derivatives of succinic acid, itaconic acid [19, 20], vanillin [21, 22], natural phenolics [23], and functionalized vegetable oils [24–29]. However, while petroleum-based filled formulations with conductive, piezoresistive, or photoluminescent properties are well established [30–35], bio-based filled systems remain scarcely investigated. Notably, conductive fillers such as CNTs have been dispersed in polyglycerol-based acrylic monomers [36], where glycerol, derived from vegetable oils [37] or microbial fermentation [38], serves as a versatile bio-based precursor.

Developing bio-based conductive 3D-printed materials is particularly attractive for applications ranging from electronics to medicine. Incorporating conductive fillers allows the creation of components with significant electrical conductivity [39–44], enabling, for example, thermotherapy devices that exploit the Joule effect for localized heating in medical treatments [45, 46] or custom conductive pathways in electronics [47].

Within this framework, we investigated acrylated polyglycerol formulations for DLP 3D printing. Electrical conductivity was imparted by dispersing silver, copper, nickel powders, and recycled carbon fibers (RCF). The printing processes were optimized, and the resulting objects were characterized by DMTA, conductivity analysis, and thermal imaging to assess Joule heating performance. Moreover, a ring-shape thermotherapy device was developed as proof-of-concept. The manufacturing of bio-derived acrylated polyglycerol composites with the above-mentioned fillers has never been studied previously. Additionally, in the direction of current research and policy trends, the use of RCF coming from industrial waste emphasizes the circular economy perspective. As far as the authors know, this work is the first demonstration of bio-based, electrically conductive DLP composites applied to functional devices.

2 Materials and method

2.1 Materials

All the formulations were made using a bio-based polymeric matrix precursor, polyglycerol-based acrylic monomer, Syntech SA Serie SA-TE12, procured from Sakamoto Yakuhin Kogyo Co., Ltd. (Osaka, Japan), with a molecular weight of 1200 g/mol. The general chemical structure for SA-TE12 monomer is represented in Fig. 1 [36].

The radical photoinitiator used was diphenyl(2,4,6-trimethylbenzoyl) phosphine oxide, purchased by Sigma Aldrich (Milan, Italy) under the trade name of BAPO.

Additionally, various types of fillers were introduced in different contents. The selected fillers are nickel (Ni), copper (Cu), and silver (Ag) under powder form, and mechanically recycled carbon fibers (RCF). All the metallic fillers, provided by Sigma-Aldrich, present different granulometry: 5–8 µm for silver powder ($\sigma_{Ag} = 6{,}30 \times 10^7$ S/m), 10–25 µm for copper powder ($\sigma_{Cu} = 5.96 \times 10^7$ S/m) and 3–7 µm for nickel ($\sigma_{Ni} = 1.43 \times 10^7$ S/m) [48]. The RCF were recovered from dismissed composite parts by mechanical milling, performing 10 milling cycles at 3000 rpm with a sieve size of 2 mm using a Pulverisette 19 equipment from Fritsch. SEM images of fillers are visible in Fig. 2.

2.2 Formulations preparation

A total of 15 formulations were investigated in this work. Table 1 reports the studied formulations.

In each formulation, 1 phr of radical photoinitiator (BAPO) was added to SA-TE12. All formulations were placed in a sonication bath for 10 min at 60 °C to properly dissolve and homogenize the photoinitiator into the resin since it is in fine powder form. Afterward, a THINKYMIXER ARE-250 planetary mixer was used to homogeneously distribute fillers in the monomer and degas the formulations, according to the following program: 1 min mixing and then 1 min degassing at 1600 rpm, 1 min mixing

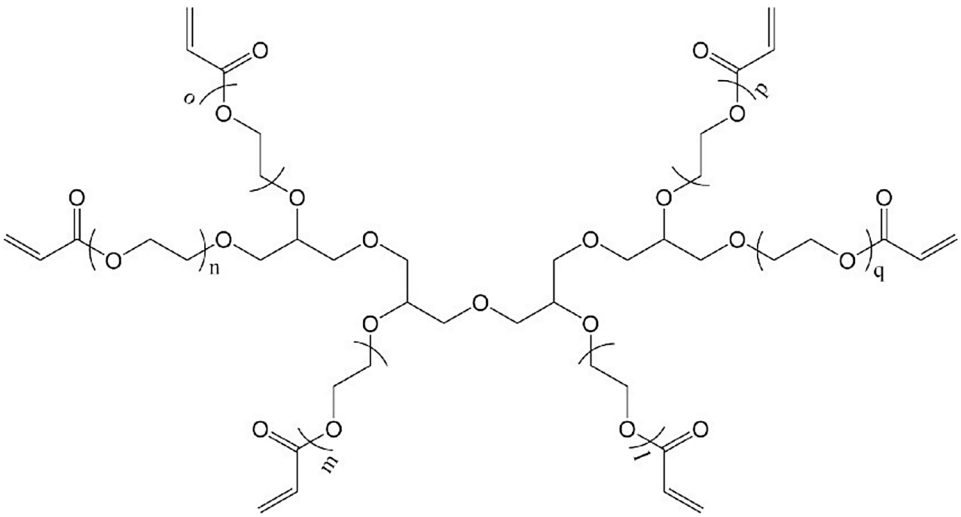

Fig. 1 Chemical structure of SA-TE12 monomer

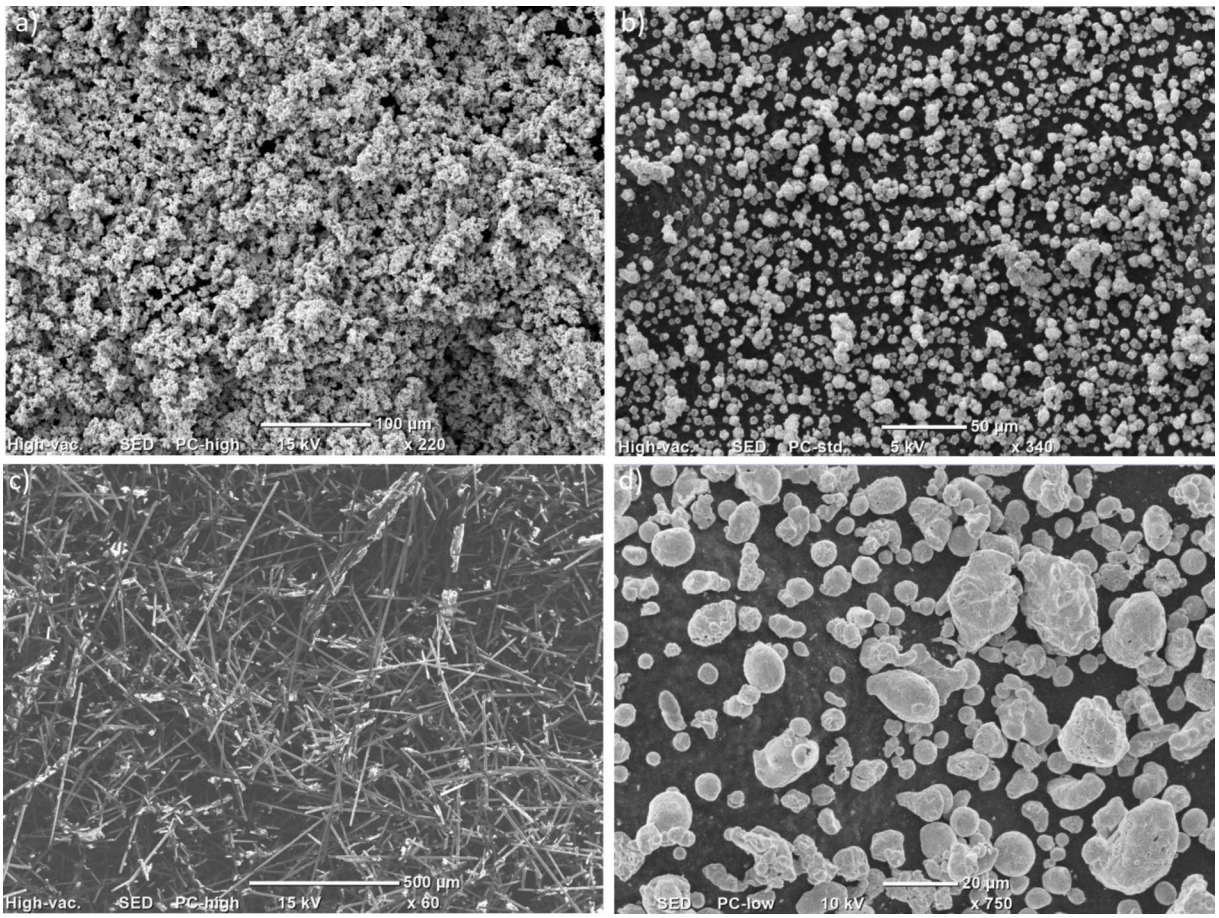

Fig. 2 SEM images of Ag (**a**), Ni (**b**), RCF (**c**) and Cu (**d**) used as fillers

and then 1 min degassing at 1800 rpm, and finally 2 min mixing at 2000 rpm.

2.3 Vat photopolymerization 3D printing

For 3D printing, a Phrozen Sonic Mighty 4 K printer was used. The printer was modified by Sharebot, having created an aluminum volume reducer for the VAT and a suitable reduced build surface. It is a DLP type printer with a digital

Table 1 List of formulations analyzed

Filler content	Type
0%wt	Pristine SA-TE12
5%wt	RCF
9%wt	RCF
20%wt	Ag, Ni, Cu
33%wt	Ag, Ni, Cu
43%wt	Ag, Ni, Cu
50%wt	Ag, Ni, Cu

Table 2 Constant printing parameters

Parameter	Value
Layer height (µm)	50
Bottom layer count	2
Lift distance (mm)	8
Lift speed (mm/min)	60
Retract speed (mm/min)	150

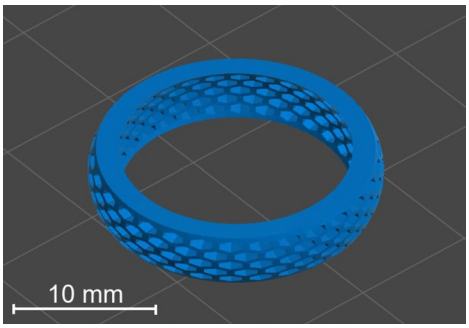

Fig. 3 CAD model of a honeycomb ring for thermotherapy

mask, exploiting LED light source emitter with a wavelength of 405 nm. The resolution in the xy plane is 52 µm while in the z plane it is in the range of 10–300 µm. The build platform used has a surface printable area of 50 × 50 mm^2.

Printing parameters, such as the irradiation time of each layer, the layer thickness, and the waiting time between irradiations, can be varied using the printer-compatible software, called Chitubox Basic. These parameters were varied according to the formulation used, basically considering the type and content of filler present, as will be reported in Sect. 3.2. Other parameters remained fixed for each of the formulations, particularly the ones shown in Table 2.

18 × 8 × 1 mm^3 samples were 3D-printed for DMTA and electrical conductivity tests. In addition, a complex geometry wearable ring was obtained to demonstrate the excellent printability of the designed formulations, while serving as a proof-of-concept device for thermotherapy applications. The CAD model of the proof-of-concept is reported in Fig. 3.

After printing, each specimen was immersed in isopropanol and placed in a sonication bath for 5 min to remove any uncured resin residue. Finally, post-curing was performed on the test specimens using the Phrozen Curing Station, with a wavelength of 405 nm.

To perform the post-curing phase, the samples were placed inside the UV lamp in the center of the rotating plate for approximately 15 min.

2.4 Characterizations of liquid formulations

2.4.1 FT-IR spectroscopy

IR spectroscopy was used to measure the conversion of the resin upon exposure to UV light. In particular, since the used monomer has acrylate groups, a lowering of the peak characteristic of acrylates after UV exposure is expected. The conversion was calculated using Eq. (1) [49, 50].

$$Conversion(\%) = \frac{\left(\frac{A_{functional}}{A_{reference}}\right)_{t=0} - \left(\frac{A_{functional}}{A_{reference}}\right)_{t}}{\left(\frac{A_{functional}}{A_{reference}}\right)_{t=0}} \cdot 100 \quad (1)$$

where $A_{\text{functional}}$ is the peak area of the functional group under investigation during the test, specifically the acrylate group (centered at around 1680 and 1580 cm^{-1}), and $A_{\text{reference}}$ is the area of the peak used as a reference, the carbonyl one in this case, centered at around 1780 and 1680 cm^{-1} [51]. With t = 0 and t, the pre- and post-UV irradiation times are indicated, respectively.

The Thermo ScientificTM NicoletTM iS50 FT-IR spectrometer and OmnicTMSpectra software were used to conduct this analysis, and the Hamamatsu LC8 lamp was adopted for conducting the photo-crosslinking. The formulations were deposited on a silicon substrate with a spreader bar, in the form of films approximately 12 µm thick. Subsequently, the IR spectrum of the test sample was recorded prior to UV exposure (pre-curing, t = 0 s). After that, each film was irradiated with the UV lamp for 10–180 s with a resulting irradiation energy of about 30 mW/cm^2. After each irradiation, the IR spectrum of the sample was again recorded by noting the irradiation time, t, in seconds. In a second period, the conversion percentage of the samples is followed and reported as a function of the exposure time, from 0 to 180 s.

2.4.2 Photo-DSC

The photo-DSC analysis was performed with the Mettler TOLEDO DSC-1 instrument and the Hamamatsu LC8 type mercury lamp, with a wavelength of 365 nm. For this test, the lamp was used at 10% of the total intensity, with a resulting irradiation energy of 30 mW/cm^2. For each test, 5–10 mg of liquid resin was placed inside an aluminum crucible with a volume of 40 µL, while an empty crucible was used as

a reference. The tests were carried out at a temperature of 25 °C, in a nitrogen atmosphere with a flow rate of 40 ml/min, and three samples were analyzed for each formulation. The cycle to which the sample was subjected during the test consisted of two steps, each characterized by 2 min of lamp off to homogenize the temperature and the atmosphere of the chamber, followed by 1 min of UV irradiation. The second step was performed to obtain the baseline. This second curve obtained was subtracted from that of the first step, in order to obtain a curve related only to the light-curing of the sample. In this way, graphs of the specific heat flow [W/g] as a function of time [s] were obtained. The height of the peak (h_{peak}) is proportional to the polymerization rate, so the higher this value, the faster the polymerization kinetics. The enthalpy change (ΔH) is obtained by integrating the curve. The analysis was conducted on 3 samples for each formulation to subsequently have a weighted average over a certain standard deviation of the values obtained.

2.4.3 Rheology

The rheological properties of the thermoset precursor resin were analyzed using an Anton Paar MCR302 parallel plate rheometer. Viscosity was assessed to determine the formulations' suitability for 3D printing. Two metallic plates with a 25 mm diameter and a 1 mm gap were used. Viscosity readings were taken across a shear rate range from 0.01 to 1000 s^{-1}.

2.4.4 Jacobs working curve

Jacobs curves were obtained from material testing conducted on the DLP printer using a light intensity of 3.3 mW/cm^2 while varying exposure times. Resins were printed directly onto the VAT without a platform, subjected to different exposure durations, rinsed with solvent, and their thicknesses were measured to determine the curing depth at each exposure level. Derived from the Lambert–Beer law, the Jacob equation generates a model describing the working curves, offering essential parameters for understanding the UV-curing process in 3D printing [52, 53].

Equation (2) was applied to calculate the critical exposure energy (E_c) and the energy required to cure a layer with a thickness of 50 µm.

$$C_d = D_p \cdot \ln\left(\frac{E}{E_c}\right) \tag{2}$$

where C_d is the curing depth at given energy exposure E, D_p is the penetration depth of the light into the resin, and E_C is the critical energy exposure to have gelation [52].

2.5 Characterizations on the 3D-printed samples

2.5.1 DMTA

The Dynamic Mechanical Thermal Analysis (DMTA) was conducted using the Triton Technology instrument under tension mode with the application of a uniaxial stress, with a frequency of 1 Hz on 18 × 8 × 1 mm^3 specimens. Tests were conducted using liquid nitrogen to cool the chamber to approximately − 30 °C and were terminated when the rubbery plateau was reached, with a heating rate of 3 °C/min. The glass transition temperature (T_g) was taken as the maximum of tanδ curves.

2.5.2 Gel content

The gel content (%gel) analysis was carried out by measuring the weight loss of on 18 × 8 × 1 mm^3 3D-printed samples (approximately in a weight range of 150–200 mg) after immersing them in chloroform for 24 h at room temperature. Following the immersion, the samples were dried 24 h at air at room temperature, with an additional drying step at 60 °C for 5 h to eliminate any remaining solvent. The insoluble fraction was calculated using Eq. (3). All tests were conducted in triplicate for each composite.

$$\%gel = \frac{W_1}{W_0} \cdot 100 \tag{3}$$

where W_1 is the weight after the immersion in the solvent and W_0 is the initial weight of the sample.

2.5.3 SEM

SEM analyses were conducted to investigate filler dispersion and orientation inside the polymeric matrix on the two most conductive formulations. More precisely, photos were taken with the Jeol JCM-6000 PLUS, for each sample. The analyzed surface was covered with a 10 nm thick platinum layer.

2.5.4 Electrical conductivity analysis and Joule effect evaluation

Conductivity and Joule effect analysis were performed on samples like those for DMTA, as discussed on Sect. 2.3, for each formulation.

The electrical conductivity tests were carried out by using a Keithley 2410 source-meter. The dimensions of the specimens were 18 × 8 × 1 mm^3. Silver conductive paint was used in two 18 × 1 mm^2 opposite faces of the specimen to minimize contact resistance. Here, the electrical resistance

(R) was calculated from the voltage intensity (V–I) slope, considering Ohm's law, by sweeping the voltage from 0 to 3 V. Then, the electrical conductivity (σ) was calculated from Eq. (4), where L is the distance between the electrodes, and A the cross-sectional area.

$$\sigma = L/(A \cdot R) \tag{4}$$

The Joule heating characterization was carried out by using a FLIR T530 thermal camera while applying voltage ranging from 1 to 15 V using the same source-meter equipment and specimens as in the electrical characterization tests. Here, the maximum and average temperatures, T_{max} and T_{av}, respectively, were recorded once the temperature was stable on time for each applied voltage. Furthermore, the homogeneity in Joule heating (H) was calculated from Eq. (5).

$$H = 1 - (T_{max} - T_{av})/T_{av} \tag{5}$$

3 Results and discussions

3.1 Characterization of curing process

3.1.1 FT-IR spectroscopy

The liquid formulations were subjected to infrared spectroscopy, collecting spectra after different exposure times: 0, 10, 20, 30, 60, 120, and 180 s of UV irradiation. Figure 4 shows the spectra of SA-TE12 with 50%wt Ag as an example. The spectrums of the other formulations were registered and used for obtaining the conversion curves by means of Eq. (1).

The conversion percentage was calculated using Eq. (1). In Fig. 5 the conversion curves are reported as a function of the irradiation time for all the investigated formulations, while Table 3 shows the conversion values after 180 s of UV irradiation for each formulation.

As can be seen from the above values, the conversion rate slightly decreases as the filler content increases in the photocurable formulation. Two factors can be responsible for this result. The first one is the increase in the formulation viscosity as the filler content increases. This can hinder the forming polymer chain motion, affecting the rate of photo crosslinking. The second aspect is related to the lower absorption of UV light by the photoinitiator since an increase in the filler content correlates with a greater shielding and absorption effect by the latter. In particular, the table shows that the same weight content, but different fillers correspond to different UV absorptions. RCF appears to be the filler with the greatest UV absorbing and shielding effect, as lower contents (maximum 9%wt) result in lower conversion values than those obtained with metal powder fillers but with significantly higher contents (20–50%wt). This can be ascribed to the higher aspect ratio, lower density, and black color of the RCF compared to metallic fillers.

3.1.2 Photo-DSC

The kinetic UV-curing of the different formulations was tested by photo-DSC. Figure 6 reports the evolution of the heat-flow during the irradiation time for all formulations.

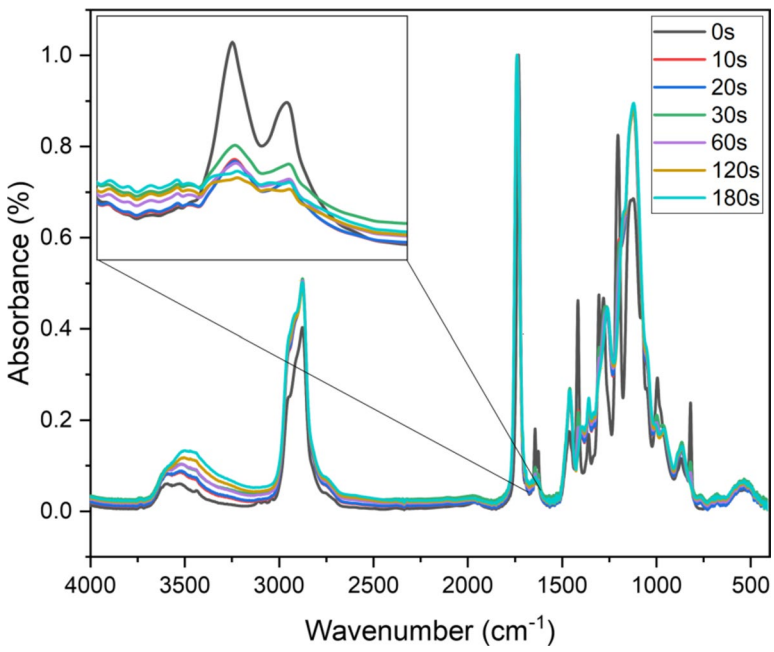

Fig. 4 SA-TE12 with 50%wt Ag powder absorbance FT-IR spectrum with magnification on acrylate's peak

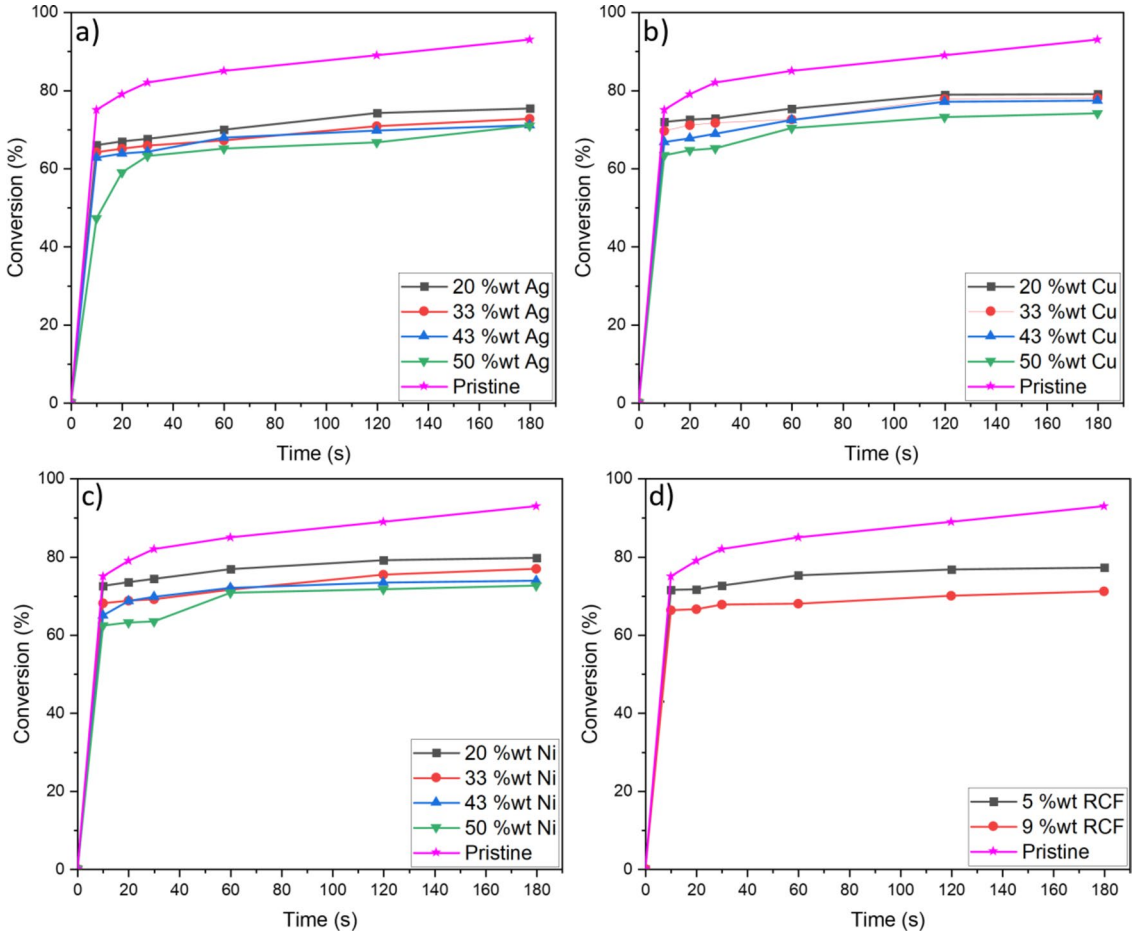

Fig. 5 Conversion curves as a function of UV exposure time of SA-TE12 pristine and when varying the content of Ag (**a**), Cu (**b**), Ni (**c**), and RCF (**d**) in the formulation

Additionally, Table 4 shows the average values of h_{peak} (maximum value of the curve), and the enthalpy change (ΔH), calculated as the integral of the curve. The time to peak (t_{peak}) remains approximately constant, around 5 s, for all the analyzed formulations.

Figure 6 and the Table 5 show that, as the content of filler increases, the value of h_{peak} and ΔH decrease. Knowing that the value of h_{peak} is related to the polymerization rate [49], it is possible to state that an increase in the filler content leads to a decrease in the speed and reactivity of the UV-curing process, also evidenced by the decrease in the change in enthalpy of photopolymerization. In fact, the inclusion of fillers significantly reduces both h_{peak} and ΔH compared to the pristine resin. This reduction suggests that fillers hinder the photopolymerization process by absorbing or scattering UV light, reducing light penetration and thus acrylate conversion. Furthermore, fillers act as a physical barrier to monomer diffusion, limiting crosslinking. Again, formulations reinforced with metallic fillers showed a similar behavior. On the contrary, RCF reinforced formulations showed a higher decrease in both h_{peak} and ΔH considering the lower filler content. These results agree with the FT-IR data, supporting the findings concerning the higher UV shielding effect of RCF fillers.

3.2 DLP 3D printing

3.2.1 Rheology

Rheological measurements were carried out to determine which formulations are suitable for the DLP 3D printing process. As mentioned in the literature, the viscosity values that fit for DLP printing are between 0.2 and 10 Pa·s, while the shear rate range characteristic of the process is between 5 and 20 s^{-1}[27, 36, 54]. Figure 7 shows the viscosity curves as a function of the shear rate applied for all the formulations analyzed. The ranges of both viscosity and shear rate suitable for DLP 3D printing are reported as a pale green area in all the plots.

From Fig. 7, it can be established that all the formulations in the study turn out to be largely printable. In addition to the Figure, the viscosity is reported in Table 5 for all the

Table 3 Degree of conversion after 180 s of UV irradiation for all the investigated formulations

Pristine formulation					
Conversion (%)					
86					
Reinforced formulations					
Filler content (%wt)	Cu Conversion (%)	Ag Conversion (%)	Ni Conversion (%)	Filler content (%wt)	RCF Conversion (%)
20	79	75	80	5	77
33	78	73	77		
43	77	71	74	9	71
50	74	71	73		

formulations at a shear rate of 5 s^{-1}. It is noticeable that viscosity increases as the conductive filler content increases. As expected from the previous analyses, and confirming the reasons given above, the formulations containing RCF were the most viscous. Nevertheless, all formulations remained within the indicated limits of printability.

3.2.2 Jacobs working curve

Figure 8 presents the Jacobs working curves in logarithmic scale, which allows for analyzing the polymerization behavior during the DLP 3D printing process. The slope of these curves indicates the depth of penetration (D_P), while the x-axis intercept indicates the critical exposure (E_C).

As summarized in Table 6, increasing the filler content leads to a higher E_C, signifying reduced reactivity. This observation aligns with findings from FT-IR and photo-DSC analysis. Formulations with higher filler concentrations exhibit lower curing depths (C_d) when examining the curing depth at a constant energy level. This effect can be attributed to the higher viscosity of the resins and the UV shielding influence of fillers, which hinder light absorption by the photoinitiator at the printing wavelength. In fact, by increasing the filler content, the slope of the curve decreases, thus indicating a decrease in the D_P in the resin, since the UV light is highly scattered and absorbed by the filler. The effect is also reflected in the exposure times required to cure a 50 µm thick layer, as shown in Table 6. Notably, formulations reinforced with RCF demand longer exposure times to achieve similar curing depths compared to those with metallic fillers. This can be attributed to the higher UV shielding capacity and increased viscosity of RCF-reinforced resins, as previously discussed.

3.2.3 Printing parameters

The printing parameters shown in Table 7 were used during the printing phase. These parameters were based on the type of formulation, content, and type of filler, according to the Jacobs working curves and the empirical evaluation during printing trials.

As previously mentioned, it is noticeable that all the printing parameters shown in Table 7 must be increased to enable a successful printing process when increasing the filler content. This is due to the higher resultant viscosity of the formulation and the increase in UV shielding when increasing the filler content. Furthermore, the type of filler also plays a role in the printing parameters. More specifically, different settings were required for RCF containing formulations due to the large viscosity increment and the higher UV shielding effect, according to FT-IR, photo-DSC, rheological, and Jacobs working curve characterization.

In particular, the exposure time of the initial layers (bottom exposure time) is separated from the exposure time of a generic layer. In fact, to allow adhesion between two dissimilar interfaces, that of the metal platform and the composite one of the objects under construction, the exposure time of the first 2 layers is significantly longer than that of

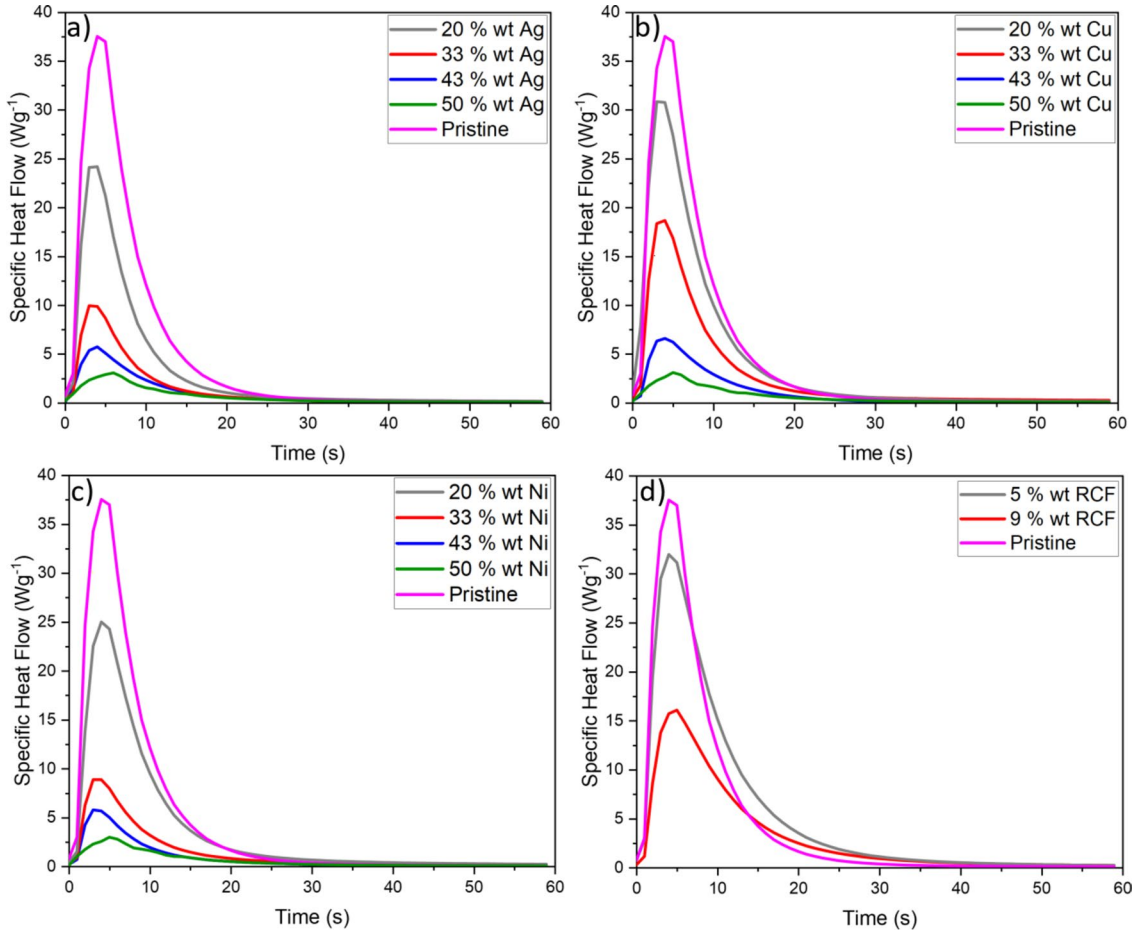

Fig. 6 Specific heat flow as a function of UV-exposure time of SA-TE12 pristine and varying the content of Ag (**a**), Cu (**b**), Ni (**c**), and RCF (**d**) in the formulation

Table 4 average values of h_{peak} and ΔH characteristic of the studied formulations

Pristine formulation									
	h_{peak} (W/g)			ΔH (J/g)					
	46 ± 5			333 ± 9					
Reinforced formulations									
Filler	Cu		Ag		Ni		Filler	RCF	
content (%wt)	h_{peak} (W/g)	ΔH (J/g)	h_{peak} (W/g)	ΔH (J/g)	h_{peak} (W/g)	ΔH (J/g)	content (%wt)	h_{peak} (W/g)	ΔH (J/g)
20	31 ± 1	295 ± 23	25 ± 1	254 ± 10	24 ± 1	248 ± 10	5	32 ± 2	315 ± 19
33	18 ± 1	192 ± 16	10 ± 1	183 ± 11	9 ± 1	185 ± 15			
43	7 ± 1	85 ± 9	6 ± 2	74 ± 3	6 ± 1	67± 8	9	16 ± 1	192 ± 12
50	3 ± 1	32 ± 3	3 ± 1	36 ± 3	3 ± 1	33 ± 3			

Table 5 Viscosity values at a shear rate of 5 s^{-1} of the studied formulations

Pristine formulation					
Viscosity (Pa·s)					
0.18 ± 0.02					
Reinforced formulations					
Filler Content (%wt)	Cu Viscosity (Pa·s)	Ag Viscosity (Pa·s)	Ni Viscosity (Pa·s)	Filler content (%wt)	RCF Viscosity (Pa·s)
20	0.23 ± 0.01	0.36 ± 0.05	0.27 ± 0.06	5	2.20 ± 0.40
33	0.24 ± 0.02	0.41 ± 0.07	0.50 ± 0.01		
43	0.29 ± 0.04	0.58 ± 0.01	0.51 ± 0.03	9	4.60 ± 0.90
50	0.50 ± 0.10	0.93 ± 0.02	0.64 ± 0.05		

the subsequent layers. Furthermore, the light off delay is the waiting time between each exposure. It must be increased with the increase in the resin viscosity to permit a homogeneous spread of the formulation in the VAT after each UV curing step. These two parameters have been empirically found.

As already introduced, crosslinked samples were obtained through DLP 3D printing for the analysis of thermo-mechanical properties by means of DMTA, for the investigation of thermo-electrical properties and to investigate the feasibility of printing complex objects.

3.2.4 DMTA

The DMTA analysis was carried out on three 3D-printed samples for each formulation. Figure 9 shows the averages of tanδ curves and storage modulus (E′) as a function of temperature, for all the formulations treated.

Table 8 shows how the addition of various fillers, Ag, Cu, Ni, and RCF, affects the glass transition temperature T_g and the storage modulus in the rubbery plateau, E′ (T_g + 50 °C).

As visible from Table 8, the pristine SA-TE12 polymer has a T_g of approximately 54 °C while the addition of fillers generally lowers the T_g. This reduction can be attributed to the decrease of the double bond conversion, as measured from FT-IR and photo-DSC analysis, thus lowering T_g.

On the other hand, all metallic reinforced composites show an increase in T_g as filler content increases from 20%wt to 50%wt. However, at an intermediate filler content (33%wt or 43%wt, depending on the filler), T_g tends to stagnate at relatively lower values. This behavior can be attributed to the UV shielding effect, which reduces the degree of double bond conversion during curing. At these levels, the reduced curing efficiency is not sufficiently counterbalanced by the filler's ability to restrict chain mobility in the polymeric network, providing a stiffening effect. At higher filler content (50%wt) the content becomes high enough that the chain mobility restriction dominates over the UV shielding effect. As a result, T_g increases significantly at 50 %wt, showing the strong influence of the filler that starts to act as a reinforcement on the thermal and mechanical properties, despite a reduction in curing efficiency. In summary, at intermediate filler levels, the prominent effect is a reduced curing (due to UV shielding effect) over chain mobility restriction (due to the filler) leads to a lowering of T_g. At higher filler contents, the mobility restriction effect becomes more dominant, and it is able to balance the lower curing grade, T_g increases.

For RCF reinforced composites, the trend differs from metallic fillers in that T_g decreases as the filler content increases from 5%wt to 9%wt. Although RCF provides some hindrance to polymer chain mobility, its effect at higher filler contents (9%wt) is outweighed by the reduced crosslink density. This leads to a less rigid polymer network, contributing to the observed decrease in T_g. At 5%wt, the UV shielding effect is relatively minor, and the polymer network benefits from adequate curing. The chain mobility

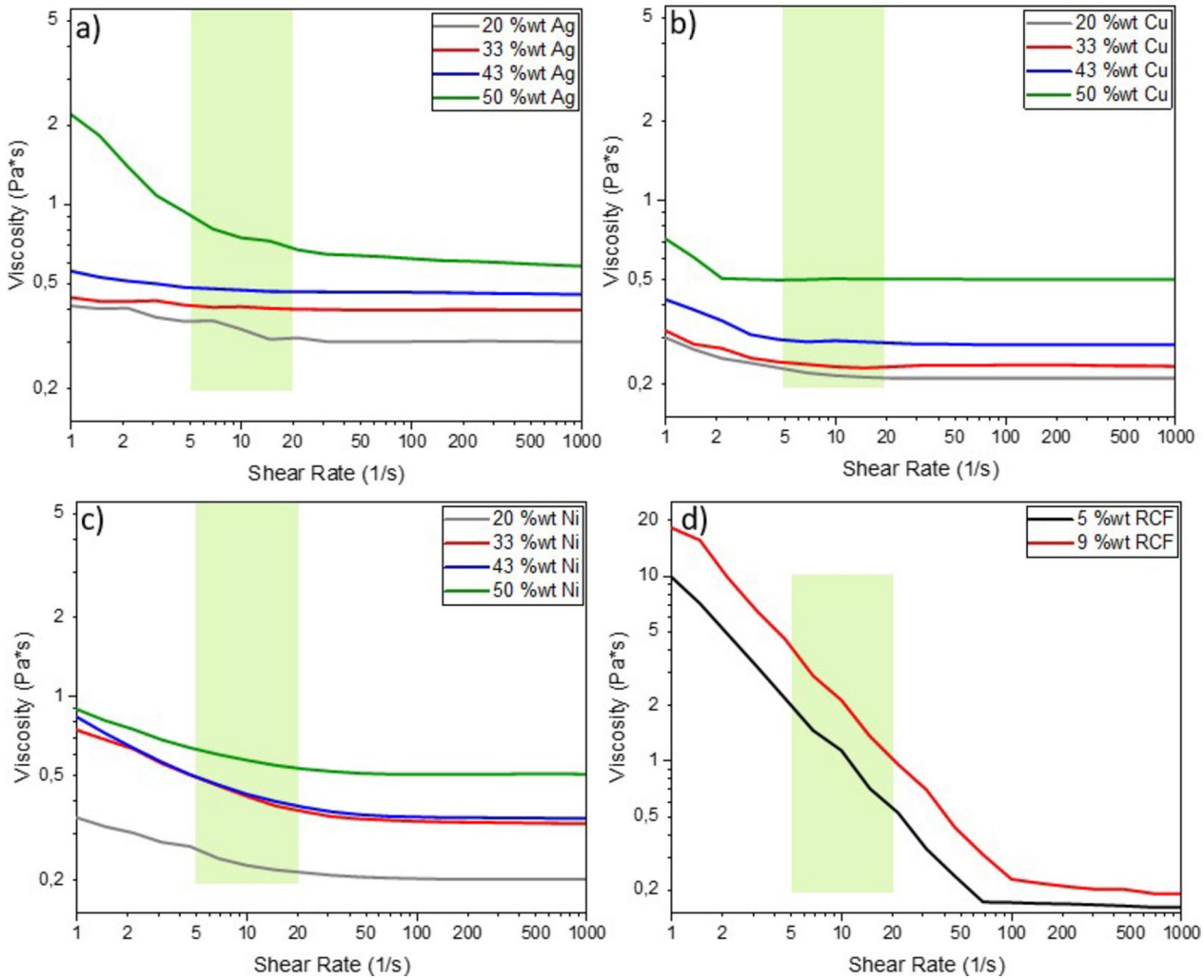

Fig. 7 Viscosity as a function of shear rate for SA-TE12 at different contents of Ag (**a**), Cu (**b**), Ni (**c**), and RCF (**d**), the printable area is highlighted in green

restriction imposed by the RCF at this content level contributes to a higher T_g.

Regarding the storage modulus registered at the rubbery plateau, E′(T_g + 50 °C), for 20%wt to 43%wt of metallic fillers, E' values remain relatively stable and constant, with a value approximately equal to the pristine sample. On the other hand, at 50%wt content of metallic fillers, a significant reduction in E′(T_g + 50° C) occurs, likely due to the excess filler disrupting the polymer matrix's uniformity and flexibility in the rubbery state. The highest improvement of E' registered at T_g + 50 °C is obtained with the addition of RCF, particularly for 5%wt RCF. In fact, it passes from 110 MPa of the pristine resin to 461 and 220 MPa for 5%wt RCF and 9%wt RCF, respectively. This can be explained since RCF has a high aspect ratio, which means they provide a large surface area for interaction with the polymer matrix. This leads to effective stress transfer from the polymer matrix to the fibers, yielding a significant increase in mechanical strength. Even at low filler contents, RCF acts as a reinforcing agent, improving the overall modulus of the composite. In addition, the incorporation of RCF limits the mobility of polymer chains, particularly in the rubbery state. This restriction increases the modulus by reducing the flexibility and damping of the network.

3.2.5 Gel content

Gel content analysis was conducted to confirm the development of crosslinked structures responsible for forming an insoluble network. The influence of filler content on acrylate conversion, potentially limiting the establishment of a proper network, was evaluated in 3D-printed composites. The results, obtained using Eq. (3), are summarized in Table 9. High gel content values, exceeding 98%, are noticeable for all thermosetting samples, confirming the

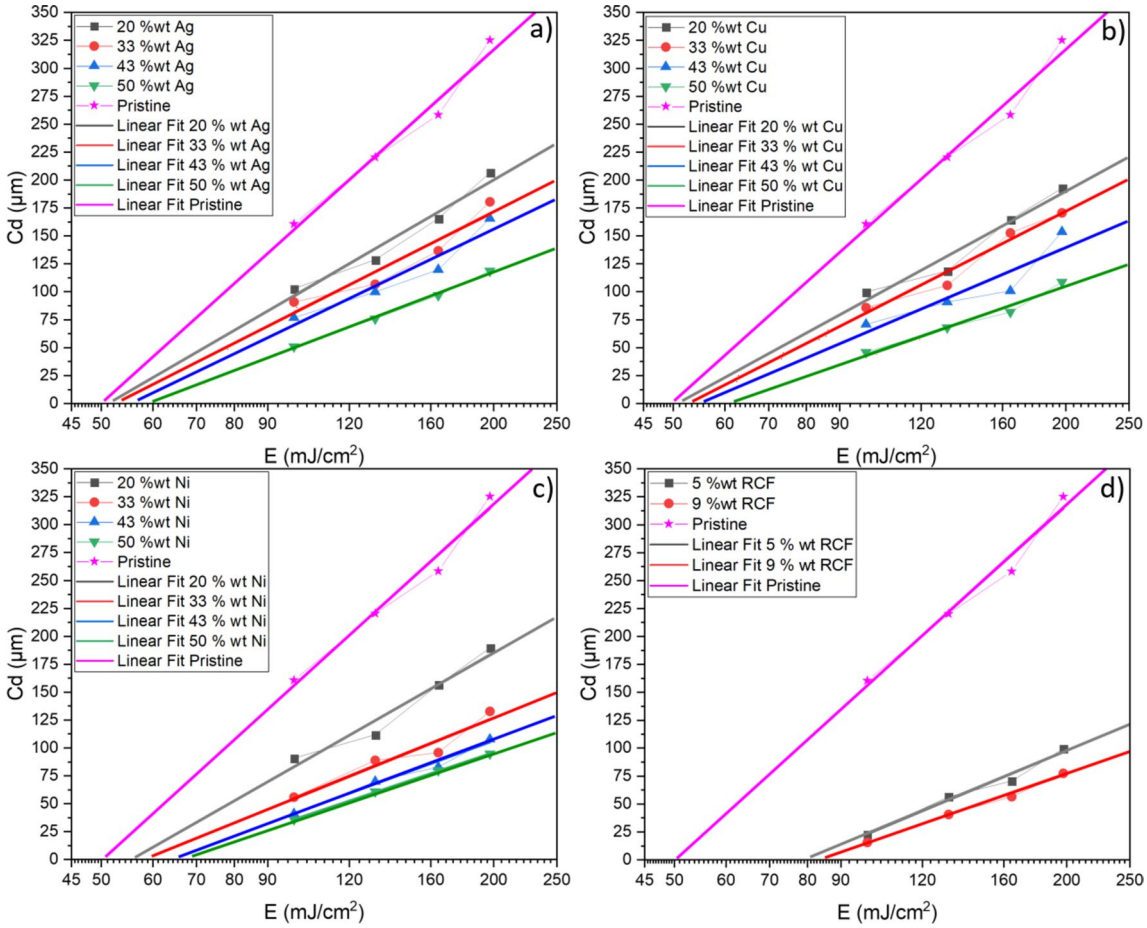

Fig. 8 Jacobs working curves for SA-TE12 pristine and at different contents of Ag (**a**), Cu (**b**), Ni (**c**) and RCF (**d**)

Table 6 Critical exposure (E_C) to obtain curing and exposure time to obtain a 50 µm layer for all the analyzed formulations

Pristine formulation									
E_c (mJ/cm²)			Time (s)						
50			19						
Reinforced formulations									
Filler	Cu		Ag		Ni		Filler	RCF	
content (%wt)	E_c (mJ/cm²)	Time (s)	E_c (mJ/cm²)	Time (s)	E_c (mJ/cm²)	Time (s)	content (%wt)	E_c (mJ/cm²)	Time (s)
20	53	22	52	21	56	24	5	80	38
33	55	23	54	23	60	29			
43	57	26	58	25	66	33	9	86	44
50	62	33	60	30	70	35			

Table 7 Printing parameters adopted as a function of the formulation type

Ag, Ni, and Cu reinforced formulations			
Filler content (%wt)	Bottom exposure time (s)	Exposure time (s)	Light off delay (s)
20	200	25	10
33	250	30	15
43	280	33	20
50	300	35	25
RCF reinforced formulations			
Filler content (%wt)	Bottom exposure time (s)	Exposure time (s)	Light off delay (s)
5	300	40	20
9	400	45	30

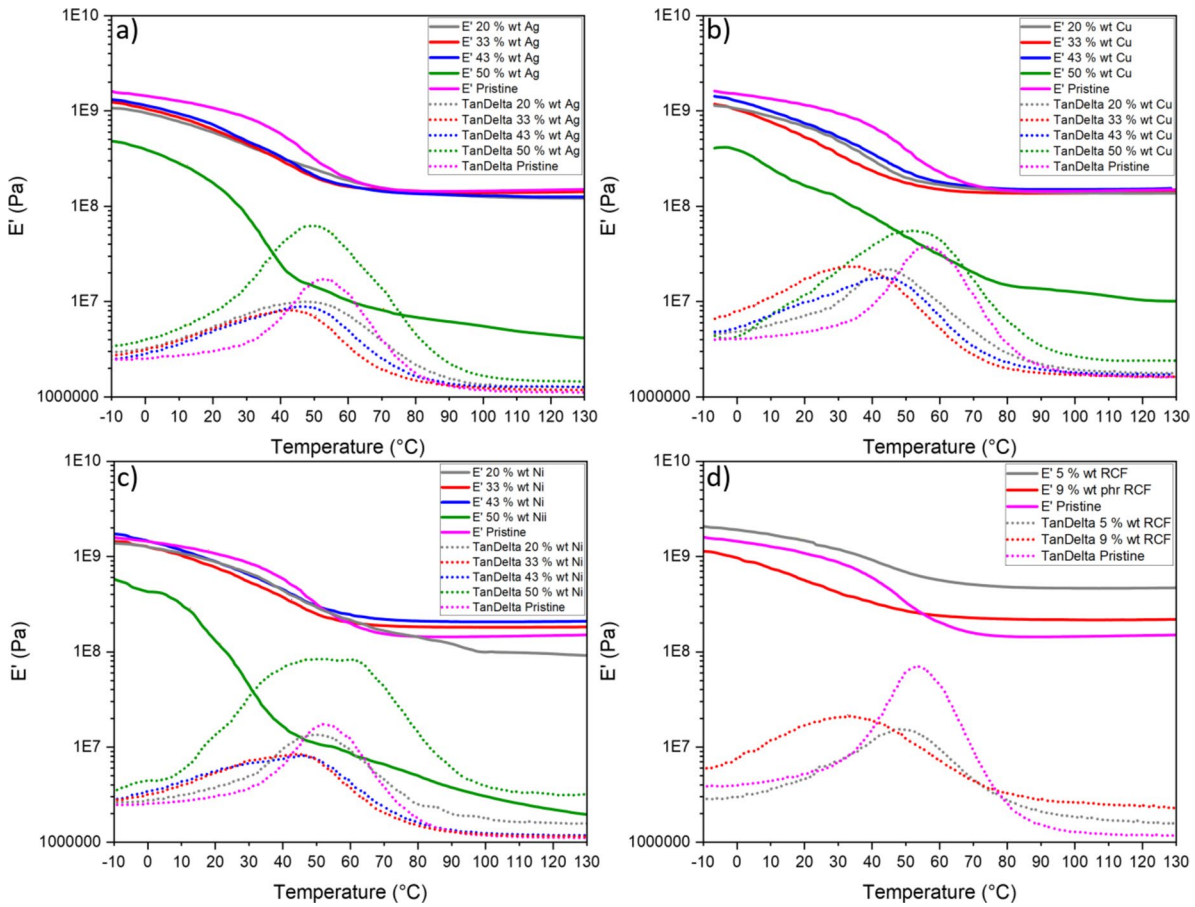

Fig. 9 tanδ and E' curves as a function of temperature for Ag (**a**), Cu (**b**), Ni (**c**), and RCF (**d**) formulations

Table 8 Values of T_g and E' in the rubbery plateau of analyzed samples

Pristine formulation									
T_g (°C)					E' (T_g+50 °C) (MPa)				
54 ± 1					110 ± 1				
Reinforced formulations									
Filler	Cu		Ag		Ni		Filler	RCF	
content (%wt)	T_g (°C)	E'(T_g+50 °C) (MPa)	T_g (°C)	E'(T_g+50 °C) (MPa)	T_g (°C)	E'(T_g+50 °C) (MPa)	content (%wt)	T_g (°C)	E'(T_g+50 °C) (MPa)
20	43±2	136 ± 2	46 ± 2	125 ± 1	49 ± 1	103 ± 1	5	49 ± 1	461 ± 3
33	33 ± 2	149 ± 1	43 ± 1	128 ± 1	43 ± 2	180 ± 1			
43	46 ± 1	137 ± 1	47 ± 1	137 ± 1	44 ± 1	205 ± 1	9	34 ± 1	220 ± 2
50	54 ± 2	12 ± 1	52 ± 2	6 ± 1	50 ± 2	3 ± 1			

Table 9 Values of %gel of 3D-printed composites

Pristine formulation					
Gel content (%)					
99.98 ± 0.01					
Reinforced formulations					
Filler content (%wt)	Cu Gel content (%)	Ag Gel content (%)	Ni Gel content (%)	Filler content (%wt)	RCF Gel content (%)
20	99.95 ± 0.01	99.97 ± 0.01	99.95 ± 0.03	5	99.96 ± 0.02
33	99.94 ± 0.02	99.96 ± 0.01	99.92 ± 0.02		
43	99.92 ± 0.01	99.88 ± 0.01	99.91 ± 0.01	9	98.20 ± 0.03
50	99.48 ± 0.01	99.40± 0.01	99.25 ± 0.01		

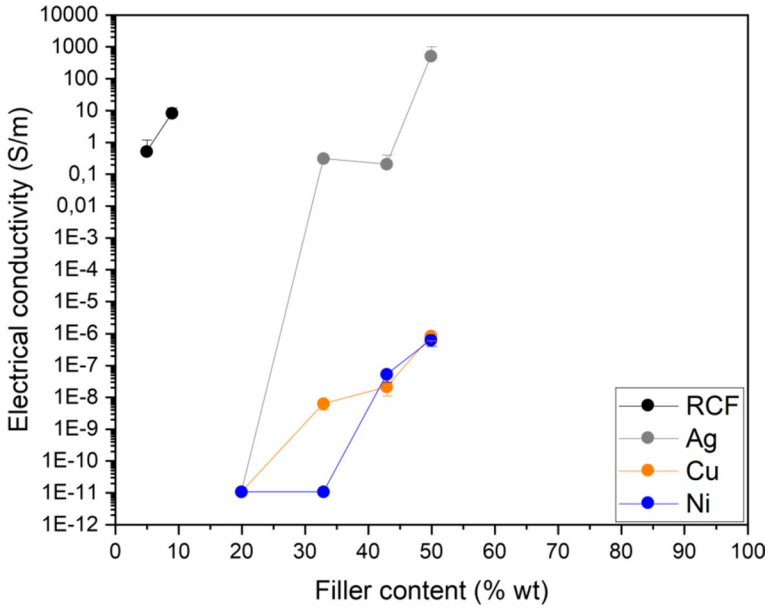

Fig. 10 Electrical conductivity of 3D-printed samples as a function of filler content and type

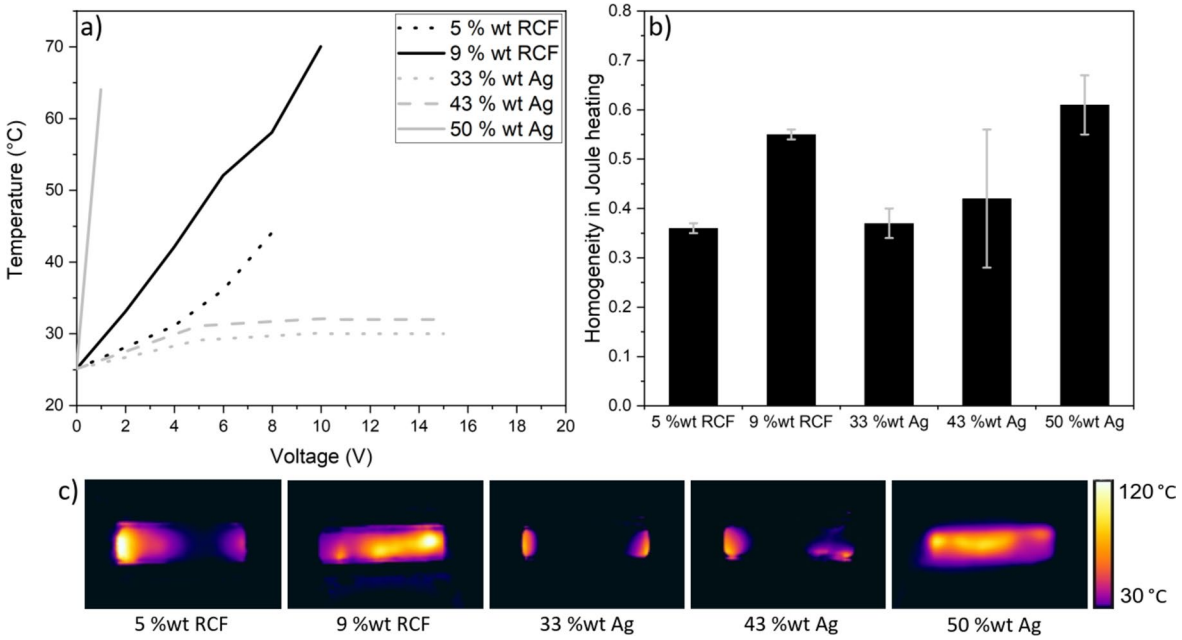

Fig. 11 Temperatures achieved by Joule heating for different samples as a function of applied voltage (**a**), homogeneity of Joule heating for different samples (**b**), thermographs of samples at maximum applied voltage (**c**)

effective formation of an insoluble network through DLP 3D printing, followed by a post-curing process.

3.2.6 Electrical conductivity and Joule effect

The electrical conductivity of all the formulations as a function of the filler content is shown in Fig. 10 and it was obtained using Eq. (4), reported in Sect. 2.5.4.

The specimens containing RCF reached the electrical percolation threshold using just 5%wt of filler, followed by the specimens reinforced with Ag and Cu (around 33%wt), and finally, those reinforced with Ni (around 43%wt). This can be ascribed to the lower density and higher aspect ratio of RCF. Moreover, from Fig. 10 it is noticeable that the highest conductivity was achieved by the 50%wt Ag due to the high filler content and the excellent conductivity of Ag. It is worth mentioning that the results obtained with the RCF are quite interesting since this conductive filler comes from waste, which promotes sustainability and circular

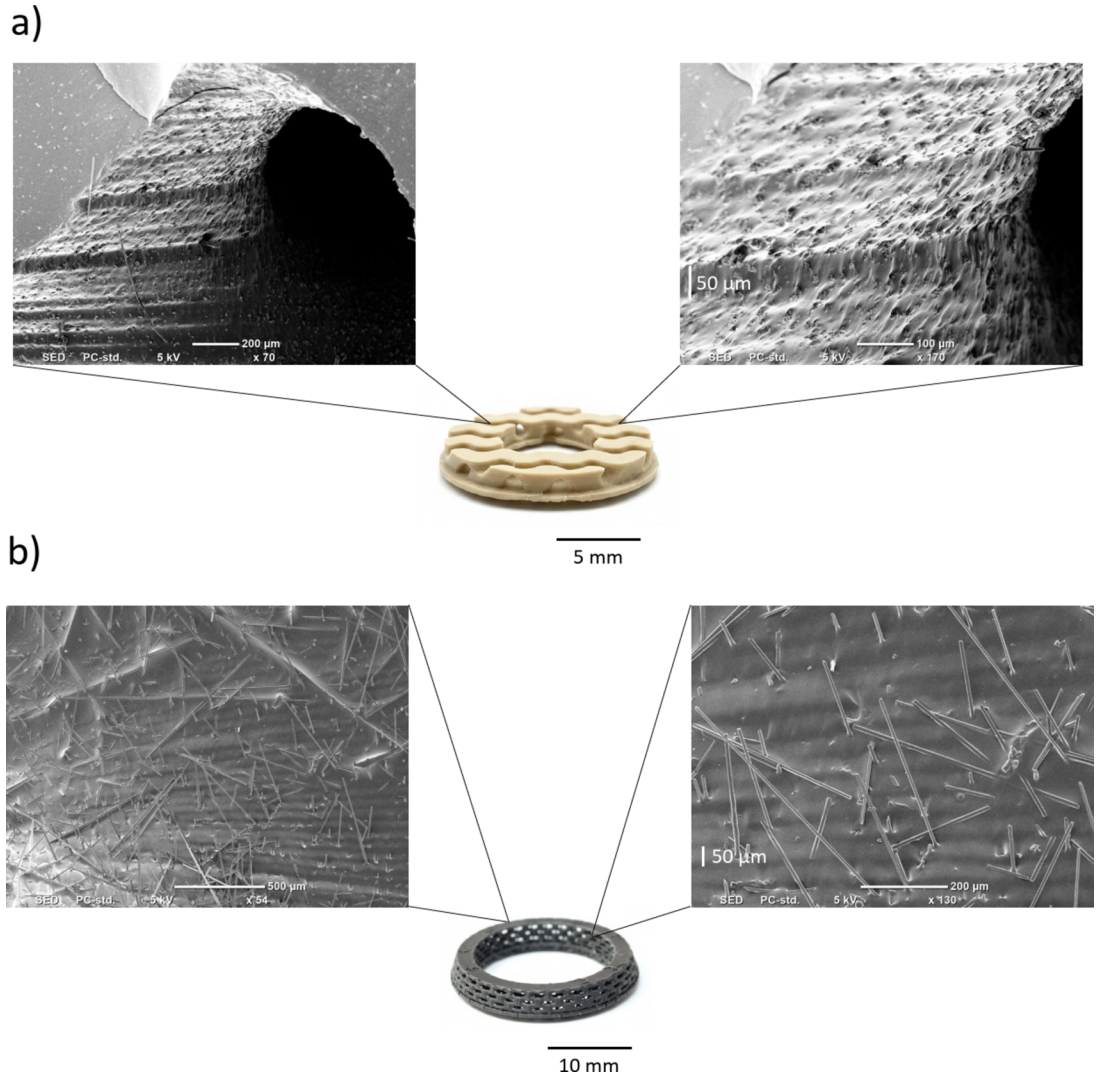

Fig. 12 SEM images of samples with 50%wt Ag (**a**) and 9%wt RCF (**b**)

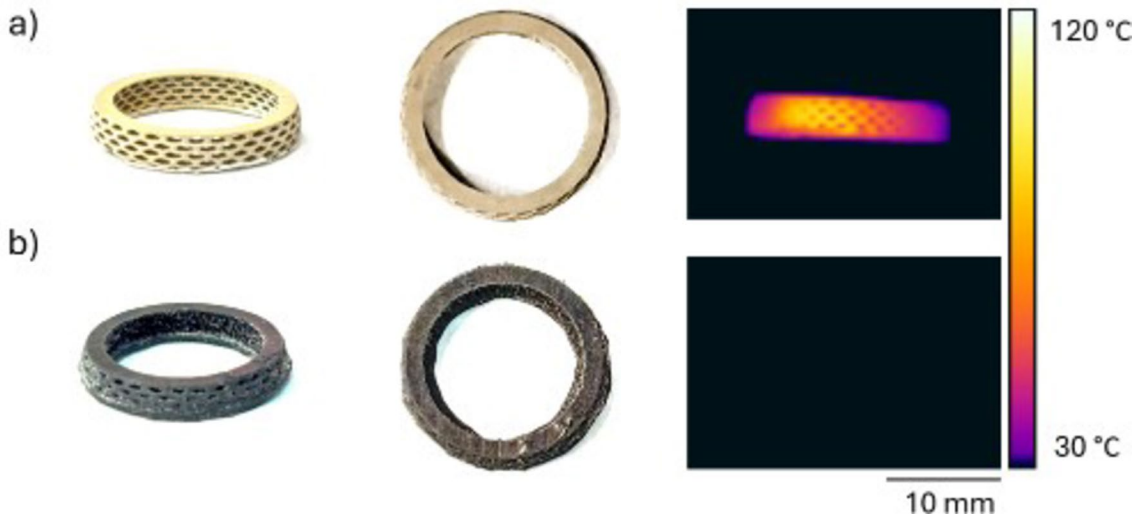

Fig. 13 Joule heating tests carried out for the proof-of-concept honeycomb rings with 50%wt Ag (**a**) and 9%wt RCF (**b**)

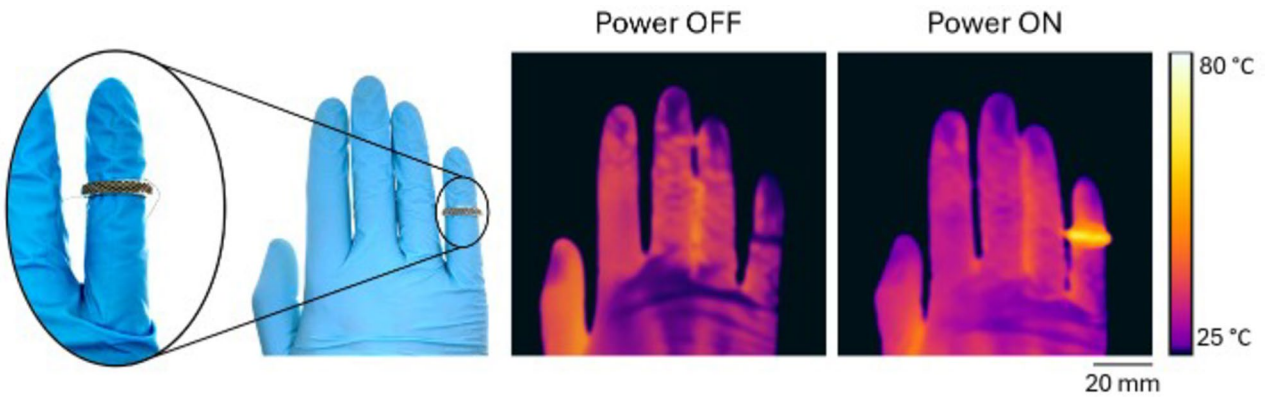

Fig. 14 Performance of the proof-of-concept ring with 50%wt of Ag powder

economy, it is cheaper than the other fillers, and a low content is needed to reach the electrical percolation threshold.

Furthermore, Joule heating was found to be directly related to the electrical conductivity, as shown in Fig. 11a. Here, the higher the electrical conductivity, the higher the temperature reached by Joule heating.

By analyzing the results in detail, just the specimens containing RCF or Ag were able to increase the temperature by Joule heating, due to their higher electrical conductivity in comparison to the ones reinforced with Cu or Ni. In fact, these specimens did not increase the temperature despite applying even 500–600 V, in comparison to the 1–10 V applied to specimens containing Ag and RCF. As a result, Cu and Ni specimens have been discarded. Nevertheless, two conditions showed the best results in terms of heating, basically due to their higher electrical conductivity. These are the 9%wt RCF, reaching temperatures over 60 °C by applying around 10 V, and the 50%wt Ag, which reached temperatures over 60 °C with just 1 V.

Furthermore, Fig. 11b shows the homogeneity in Joule heating (H), which can be calculated using Eq. (5), reported in Sect. 2.5.4.

Here, the specimens that presented a higher electrical conductivity and, therefore, higher Joule heating capability, also showed a higher H. This can be explained by the fact that these contents are above the electrical percolation threshold, so there are plenty of conductive pathways throughout the material, making Joule heating more homogeneous. On the other hand, the specimens near the electrical percolation threshold present regions that are locally more electrically conductive, and other regions that are not percolated, leading to a higher heterogeneity in Joule heating. In this sense, Fig. 11c shows thermographs of the specimens at the maximum applied voltage of each manufacturing condition, which are in total agreement with the results obtained in terms of homogeneity in Joule heating.

As reported in Fig. 12, SEM images of the two most conductive samples were obtained to show the formation of a percolative homogeneous network of conductive fillers. It is important to mention that the SEM observation allowed to see that no sedimentation or phase separation were taking place. Ag-reinforced composites presented a better dispersion than the RCF-reinforced ones. This can be attributed to the higher aspect ratio and lower density of RCF, promoting reaggregation and entanglement. However, the dispersion is good enough to present a relatively homogeneous heating, similar to the ones reinforced with Ag particles as demonstrated in Fig. 11c. Also, good bonding between the printed layers can be appreciated in Fig. 12, in addition to the layer thickness for both composites.

In addition, a Joule heating test was conducted on the proof-of-concept rings for thermotherapy to investigate the influence of geometry on the electrical performance of the sample. Once more, silver paste and copper electrodes were positioned on opposing flat surfaces to induce Joule heating through the rings. As illustrated in Fig. 13a, the silver containing ring exhibited excellent behavior, attaining average temperatures of approximately 60 °C when subjected to a limited voltage of 1–3 V. However, the RCF ring was unable to be heated by the Joule effect despite the utilization of higher voltages, as evidenced in Fig. 13b. This can be attributed to the complex intricate geometry of the rings, hindering the formation of the electrical percolation network.

Therefore, the performance of the Ag reinforced ring is illustrated in Fig. 14 while the device is worn on a finger.

It should be emphasized that 3D-printed objects can be customized to all kinds of geometries and shapes to fit any part of the body or to heat the desired region most efficiently. Considering the remarkable heating capabilities by applying low voltages, as well as the possibility of designing the device according to the patient's needs, the suitability of the developed thermotherapy devices for the proposed application was demonstrated.

4 Conclusions

The work demonstrates the feasibility of 3D-printing smart, highly conductive and eco-friendly complex geometries using Vat Photopolymerization by incorporating silver, copper, nickel powders and mechanically recycled carbon fibers into a bio-derived acrylate polyglycerol monomer that can be obtained from vegetable oils or microbial fermentation. The addition of conductive fillers increases resin viscosity and hinders printability but greatly enhances the electrical conductivity of the printed parts, enabling efficient Joule heating. A ring-shaped device was successfully fabricated as proof of concept for thermotherapy.

Among the fillers, recycled carbon fibers are particularly attractive due to their sustainability, low cost and ability to reach electrical percolation at only 5 wt%, although forming a continuous conductive network becomes difficult in very intricate geometries. The best Joule heating performance was achieved with the resin filled with 50 wt% silver, which reached about 60 °C under low applied voltages (1–3 V). The proof-of-concept produced demonstrated the feasibility of the material developed to create small thermotherapy devices with really good performance, which is a significant step toward sustainable, customized devices for these applications.

Author contribution A.Ce. and A.Co conducted the experimental procedure, data treatment, formal analysis, and wrote the main manuscrpt text. L.P. reviewed the manuscript. K.M. provided the monomer and reviewed the manuscript. A.J. and M.S. provided materials and reviewed the manuscript.

Funding Open Access funding provided thanks to the CRUE-CSIC agreement with Springer Nature. Agencia Estatal de Investigación, TED2021-131102B-C21, HORIZON EUROPE Marie Sklodowska-Curie Actions, No. 101085759 (SURE-Poly), Comunidad de Madrid, M3585, RENEW-COMP.

Data availability Data will be available upon request.

Declarations

Conflict of interest The authors declare that they have no competing interests.

References

1. Lafortune G, Fuller G, Schmidt-Traub G, Kroll C (2020) How is progress towards the sustainable development goals measured? Comparing four approaches for the EU. Sustainability (Switzerland). https://doi.org/10.3390/su12187675
2. Rogelj J, Den Elzen M, Höhne N et al (2016) Paris agreement climate proposals need a boost to keep warming well below 2 °C. Nature 534(7609):631–639. https://doi.org/10.1038/nature18307
3. Patti A, Acierno D (2022) Towards the sustainability of the plastic industry through biopolymers: properties and potential applications to the textiles world. Polymers (Basel). https://doi.org/10.3390/POLYM14040692
4. Owusu PA, Asumadu-Sarkodie S (2016) A review of renewable energy sources, sustainability issues and climate change mitigation. Cogent Eng. https://doi.org/10.1080/23311916.2016.1167990
5. Khalid MY, Arif ZU, Ahmed W, Arshad H (2022) Recent trends in recycling and reusing techniques of different plastic polymers and their composite materials. Sustain Mater Technol 31:e00382. https://doi.org/10.1016/J.SUSMAT.2021.E00382
6. Mendes-Felipe C, Oliveira J, Etxebarria I et al (2019) State-of-the-art and future challenges of UV curable polymer-based smart materials for printing technologies. Adv Mater Technol 4:1800618. https://doi.org/10.1002/ADMT.201800618
7. Yagci Y, Jockusch S, Turro NJ (2010) Photoinitiated polymerization: advances, challenges, and opportunities. Macromolecules 43:6245–6260. https://doi.org/10.1021/MA1007545
8. Sangermano M, Razza N, Crivello JV (2014) Cationic UV-curing: technology and applications. Macromol Mater Eng 299:775–793. https://doi.org/10.1002/MAME.201300349
9. Decker C (2002) Kinetic study and new applications of UV radiation curing. Macromol Rapid Commun 23:1067–1093. https://doi.org/10.1002/MARC.200290014
10. MacDonald E, Salas R, Espalin D et al (2014) 3D printing for the rapid prototyping of structural electronics. IEEE Access 2:234–242. https://doi.org/10.1109/ACCESS.2014.2311810
11. Malik A, Ul Haq MI, Raina A, Gupta K (2022) 3D printing towards implementing Industry 4.0: sustainability aspects, barriers and challenges. Ind Robot 49:491–511. https://doi.org/10.1108/IR-10-2021-0247/FULL/PDF
12. Pruksawan S, Chong YT, Zen W et al (2024) Sustainable vat photopolymerization-based 3D-printing through dynamic covalent network photopolymers. Chem Asian J 19:e202400183. https://doi.org/10.1002/ASIA.202400183
13. Shahbazi M, Jäger H (2021) Current status in the utilization of biobased polymers for 3D printing process: a systematic review of the materials, processes, and challenges. ACS Appl Bio Mater 4:325–369. https://doi.org/10.1021/ACSABM.0C01379
14. Ligon SC, Liska R, Stampfl J et al (2017) Polymers for 3D printing and customized additive manufacturing. Chem Rev 117:10212–10290. https://doi.org/10.1021/ACS.CHEMREV.7B00074
15. Porcarello M, Mendes-Felipe C, Lanceros-Mendez S, Sangermano M (2024) Design of acrylated epoxidized soybean oil bio-based photo-curable formulations for 3D printing. Sustain Mater Technol 40:e00927. https://doi.org/10.1016/J.SUSMAT.2024.E00927
16. Feng S, Cui J, Guo Y et al (2025) High performance and multi-UV curable materials adaptable photothermal nanoparticles for near-infrared-responsive digital light processing based 4D printing. Compos Sci Technol 260:110984. https://doi.org/10.1016/j.compscitech.2024.110984
17. Pal AK, Mohanty AK, Misra M (2021) Additive manufacturing technology of polymeric materials for customized products:

recent developments and future prospective. RSC Adv 11:36398–36438. https://doi.org/10.1039/D1RA04060J
18. Shah SWA, Xu Q, Ullah MW et al (2023) Lignin-based additive materials: A review of current status, challenges, and future perspectives. Addit Manuf 74:103711. https://doi.org/10.1016/j.addma.2023.103711
19. Miao JT, Peng S, Ge M et al (2020) Three-dimensional printing fully biobased heat-resistant photoactive acrylates from aliphatic biomass. ACS Sustain Chem Eng 8:9415–9424. https://doi.org/10.1021/ACSSUSCHEMENG.0C02168
20. Chiaradia V, Pensa E, Machado TO, Dove AP (2024) Improving the performance of photoactive terpene-based resin formulations for light-based additive manufacturing. ACS Sustain Chem Eng 12:6904–6912. https://doi.org/10.1021/acssuschemeng.3c08191
21. Subramaniyan S, Bergoglio M, Sangermano M, Hakkarainen M (2023) Vanillin-derived thermally reprocessable and chemically recyclable Schiff-base epoxy thermosets. Glob Chall. https://doi.org/10.1002/gch2.202200234
22. Bassett AW, Honnig AE, Breyta CM et al (2020) Vanillin-based resin for additive manufacturing. ACS Sustain Chem Eng 8:5626–5635. https://doi.org/10.1021/ACSSUSCHEMENG.0C00159
23. Ding R, Du Y, Goncalves RB et al (2019) Sustainable near UV-curable acrylates based on natural phenolics for stereolithography 3D printing. Polym Chem 10:1067–1077. https://doi.org/10.1039/C8PY01652F
24. Saraswat R, Shagun N, Dhir A et al (2024) Synthesis and application of sustainable vegetable oil-based polymers in 3D printing. RSC Sustain 2:1708–1737. https://doi.org/10.1039/D4SU00060A
25. Pezzana L, Wolff R, Stampfl J et al (2024) High temperature vat photopolymerization 3D printing of fully bio-based composites: green vegetable oil epoxy matrix & bio-derived filler powder. Addit Manuf 79:103929. https://doi.org/10.1016/j.addma.2023.103929
26. Bhanushali H, Mestry S, Mhaske ST (2023) Castor oil-based UV-curable polyurethane acrylate resins for digital light processing (DLP) 3D printing technology. J Appl Polym Sci 140:e53817. https://doi.org/10.1002/APP.53817
27. Vazquez-Martel C, Becker L, Liebig WV et al (2021) Vegetable oils as sustainable inks for additive manufacturing: a comparative study. ACS Sustain Chem Eng 9:16840–16848. https://doi.org/10.1021/ACSSUSCHEMENG.1C06784
28. Chen S, Luo Y, Xu Y et al (2021) Synthesis and characterization of cardanol-based methacrylate oligomers for three-dimensional printing resins. ACS Sustain Chem Eng 9:16316–16327. https://doi.org/10.1021/acssuschemeng.1c05689
29. Bergoglio M, Najmi Z, Cochis A et al (2023) UV-cured bio-based acrylated soybean oil scaffold reinforced with bioactive glasses. Polymers. https://doi.org/10.3390/polym15204089
30. Mendes-Felipe C, Cofano R, Garcia A et al (2023) Photocurable 3D printed anisotropic electrically conductive materials based on bio-renewable composites. Addit Manuf 78:103867. https://doi.org/10.1016/J.ADDMA.2023.103867
31. Jeon H, Wajahat M, Park S et al (2024) 3D printing of luminescent perovskite quantum dot–polymer architectures. Adv Funct Mater 34:2400594. https://doi.org/10.1002/ADFM.202400594
32. Cortés A, Cosola A, Sangermano M et al (2021) DLP 4D-printing of remotely, modularly, and selectively controllable shape memory polymer nanocomposites embedding carbon nanotubes. Adv Funct Mater 31:2106774. https://doi.org/10.1002/adfm.202106774
33. Dzisah P, Sadoh A, Ravindra NM (2019) 3D Printing of Polymer-Based Gasochromic, Thermochromic and Piezochromic Sensors. In: Minerals, Metals and Materials. Springer, Cham, pp. 1545–1561. https://doi.org/10.1007/978-3-030-05861-6_146
34. Li Y, Jiang Z, Li Y et al (2024) Flexible phase change composites with multiple colors and reversible thermochromic for temperature indication and battery thermal management. Compos Sci Technol 249:110481. https://doi.org/10.1016/j.compscitech.2024.110481
35. Önder MN, Gülgün MA, Papila M (2024) Piezoresistivity analyses of GNP-filled composite piezoresistor under cycling loading and correlation with the Monte Carlo percolation model. Compos Sci Technol 254:110641. https://doi.org/10.1016/j.compscitech.2024.110641
36. Porcarello M, Bonardd S, Kortaberria G et al (2024) 3D printing of electrically conductive objects with biobased polyglycerol acrylic monomers. ACS Appl Polym Mater 6:2868–2876. https://doi.org/10.1021/ACSAPM.3C03073
37. Ben ZY, Samsudin H, Yhaya MF (2022) Glycerol: its properties, polymer synthesis, and applications in starch based films. Eur Polym J 175:111377. https://doi.org/10.1016/J.EURPOLYMJ.2022.111377
38. Bagnato G, Iulianelli A, Sanna A, Basile A (2017) Glycerol production and transformation: a critical review with particular emphasis on glycerol reforming reaction for producing hydrogen in conventional and membrane reactors. Membranes 7(2):17. https://doi.org/10.3390/MEMBRANES7020017
39. Zhang W, Dehghani-Sanij AA, Blackburn RS (2007) Carbon based conductive polymer composites. J Mater Sci 42:3408–3418. https://doi.org/10.1007/S10853-007-1688-5/METRICS
40. Xiao AY, Tong QK, Savoca AC, Van Oosten H (2001) Conductive ink for through hole application. IEEE Trans Compon Packag Technol 24:445. https://doi.org/10.1109/6144.946492
41. Scarisbrick RM (1973) Electrically conducting mixtures. J Phys D Appl Phys 6:2098. https://doi.org/10.1088/0022-3727/6/17/316
42. Cortés A, Esperanza A, Gómez-Sánchez J et al (2024) Combining de-icing and self-healing for wind blades through an innovative multilayer coating approach. Polym Compos. https://doi.org/10.1002/pc.29252
43. Cortés A, Sánchez Romate XF, Aguilar JL et al (2022) Electrothermally triggered selective shape memory capabilities of CNT doped nanocomposites by digital light processing. Compos Sci Technol 218:109185. https://doi.org/10.1016/j.compscitech.2021.109185
44. Bragaglia M, Paleari L, Passaro J et al (2023) 3D printing of biodegradable and self-monitoring SWCNT-loaded biobased resin. Compos Sci Technol 243:110253. https://doi.org/10.1016/j.compscitech.2023.110253
45. Malanga GA, Yan N, Stark J (2015) Mechanisms and efficacy of heat and cold therapies for musculoskeletal injury. Postgrad Med 127:57–65. https://doi.org/10.1080/00325481.2015.992719
46. Yi GY, Kim MJ, Kim HI et al (2022) Hyperthermia treatment as a promising anti-cancer strategy: therapeutic targets, perspective mechanisms and synergistic combinations in experimental approaches. Antioxidants 11:625. https://doi.org/10.3390/ANTIOX11040625
47. Tsai SC, Chen LH, Chu CP et al (2022) Photo curable resin for 3D printed conductive structures. Addit Manuf 51:102590. https://doi.org/10.1016/J.ADDMA.2021.102590
48. Merck | Italy. https://www.sigmaaldrich.com/IT/it. Accessed 28 Nov 2024
49. Pezzana L, Melilli G, Delliere P et al (2022) Thiol-ene biobased networks: furan allyl derivatives for green coating applications. Prog Org Coat 173:107203. https://doi.org/10.1016/J.PORGCOAT.2022.107203
50. Bergoglio M, Reisinger D, Schlögl S et al (2023) Sustainable bio-based UV-cured epoxy vitrimer from castor oil. Polymers (Basel). https://doi.org/10.3390/polym15041024

51. Magalhães ASG, Neto MPA, Bezerra MN et al (2012) Application of ftir in the determination of acrylate content in poly(sodium acrylate-co-acrylamide) superabsorbent hydrogels. Quim Nova 35:1464–1467. https://doi.org/10.1590/S0100-40422012000700030
52. Pezzana L, Fadlallah S, Giri G et al (2024) DLP 3D printing of levoglucosenone-based monomers: exploiting thiol-ene chemistry for bio-based polymeric resins. Chemsuschem 17:e202301828. https://doi.org/10.1002/CSSC.202301828
53. Jacobs PF, Reid DT (1992) Rapid prototyping & manufacturing: fundamentals of stereolithography. 434
54. Sanchez-Rexach E, Johnston TG, Jehanno C et al (2020) Sustainable materials and chemical processes for additive manufacturing. Chem Mater 32:7105–7119. https://doi.org/10.1021/ACS.CHEMMATER.0C02008

Authors and Affiliations

Alberto Cellai[1] · Lorenzo Pezzana[1] · Kimihiro Matsukawa[2] · Alberto Jiménez-Suárez[3,4] · Marco Sangermano[1] · Alejandro Cortés[3]

✉ Alejandro Cortés
alejandro.cortes@urjc.es

Alberto Cellai
alberto.cellai@polito.it

Lorenzo Pezzana
lorenzo.pezzana@polito.it

Kimihiro Matsukawa
kimihiro.matsukawa@gmail.com

Alberto Jiménez-Suárez
alberto.jimenez.suarez@urjc.es

Marco Sangermano
marco.sangermano@polito.it

[1] Polytechnic University of Turin, Turin, Italy

[2] Kyoto Institute of Technology, Kyoto, Japan

[3] Rey Juan Carlos University, Madrid, Spain

[4] Instituto de Tecnologías Para la Sostenibilidad, Madrid, Spain